applied sciences

MDPI

Article

Neural Network Ensemble to Detect Dicentric Chromosomes in Metaphase Images

Ignacio Atencia-Jiménez [1], Adayabalam S. Balajee [2], Miguel J. Ruiz-Gómez [3,4], Francisco Sendra-Portero [3,4], Alegría Montoro [5] and Miguel A. Molina-Cabello [1,4,*]

1 ITIS Software, University of Málaga, 29071 Málaga, Spain
2 Cytogenetic Biodosimetry Laboratory, Radiation Emergency Assistance Center, Training Site, Oak Ridge Institute for Science and Education, Oak Ridge Associated Universities, Oak Ridge, TN 37830, USA
3 Departamento de Radiología y Medicina Física, Facultad de Medicina, Universidad de Málaga, 29010 Málaga, Spain
4 Instituto de Investigación Biomédica de Málaga y Plataforma en Nanomedicina—IBIMA Plataforma BIONAND, 29590 Málaga, Spain
5 Laboratorio de Biodosimetría, Servicio de Protección Radiológica, Hospital Universitario y Politécnico la Fe, 46026 Valencia, Spain
* Correspondence: miguelangel@lcc.uma.es

Abstract: The Dicentric Chromosome Assay (DCA) is widely used in biological dosimetry, where the number of dicentric chromosomes induced by ionizing radiation (IR) exposure is quantified to estimate the absorbed radiation dose an individual has received. Dicentric chromosome scoring is a laborious and time-consuming process which is performed manually in most cytogenetic biodosimetry laboratories. Further, dicentric chromosome scoring constitutes a bottleneck when several hundreds of samples need to be analyzed for dose estimation in the aftermath of large-scale radiological/nuclear incident(s). Recently, much interest has focused on automating dicentric chromosome scoring using Artificial Intelligence (AI) tools to reduce analysis time and improve the accuracy of dicentric chromosome detection. Our study aims to detect dicentric chromosomes in metaphase plate images using an ensemble of artificial neural network detectors suitable for datasets that present a low number of samples (in this work, only 50 images). In our approach, the input image is first processed by several operators, each producing a transformed image. Then, each transformed image is transferred to a specific detector trained with a training set processed by the same operator that transformed the image. Following this, the detectors provide their predictions about the detected chromosomes. Finally, all predictions are combined using a consensus function. Regarding the operators used, images were binarized separately applying Otsu and Spline techniques, while morphological opening and closing filters with different sizes were used to eliminate noise, isolate specific components, and enhance the structures of interest (chromosomes) within the image. Consensus-based decisions are typically more precise than those made by individual networks, as the consensus method can rectify certain misclassifications, assuming that individual network results are correct. The results indicate that our methodology worked satisfactorily in detecting a majority of chromosomes, with remarkable classification performance even with the low number of training samples utilized. AI-based dicentric chromosome detection will be beneficial for a rapid triage by improving the detection of dicentric chromosomes and thereby the dose prediction accuracy.

Keywords: deep learning; neural network; object detection; ensemble; biological dosimetry; dicentric chromosome; radiation

Citation: Atencia-Jiménez, I.; Balajee, A.S.; Ruiz-Gómez, M.J.; Sendra-Portero, F.; Montoro, A.; Molina-Cabello, M.A. Neural Network Ensemble to Detect Dicentric Chromosomes in Metaphase Images. *Appl. Sci.* **2024**, *14*, 10440. https://doi.org/10.3390/app142210440

Academic Editor: Yuanyuan Liu

Received: 15 October 2024
Revised: 8 November 2024
Accepted: 11 November 2024
Published: 13 November 2024

1. Introduction

Human beings are exposed to both natural and man-made sources of ionizing radiation (IR). Natural sources of IR include cosmic radiation and consumables with trace amounts of radioactivity and radon, a decay product of uranium found in water and soil at varying

concentrations. IR is used for multiple applications, including the sterilization of certain food items, medical appliances, medical diagnostic imaging, and radiotherapy for cancer. IR causes a wide spectrum of DNA lesions: single-strand break (SSB), double-strand break (DSB), base damage, mutations and DNA–protein cross-links, with their induction depending on radiation dose, dose rate and radiation quality. Among these lesions, a DSB is the most critical lesion which, when not repaired or mis-repaired, can lead to either cell death or chromosome aberrations depending on the severity of exposure. Besides these lesions, IR can also trigger the generation of reactive oxygen species (ROS) through the hydrolysis of water and ROS generation. Oxidized DNA base lesions can lead to cytotoxic and genotoxic effects. Some of the man-made sources include medical diagnostic exposures and IR treatment of various illnesses such as cancer. Additionally, nuclear power plant accidents such as Chernobyl and Fukushima Daiichi [1–3] could potentially expose several hundreds and thousands of people to substantial doses of IR.

IR exposure leads to an array of health effects, ranging from an early onset of acute radiation syndrome (ARS, hematopoietic syndrome, gastrointestinal syndrome, cerebrovascular syndrome, and cutaneous syndrome) to delayed effects of tissue degeneration and cancer. These early and delayed health effects are broadly classified into two groups: (I) deterministic effects and (II) stochastic effects. While tissue reactions like cataracts, skin reddening and ARS manifest only after exceeding a threshold dose (deterministic effects), gene mutations and cancer occur randomly without a threshold, but with the probability of incidence increasing with exposure dose (stochastic effects). Human exposure to 3.5–4 Gy of photons (X-rays and gamma rays) is expected to result in a mortality of 50% of the exposed population within 30 days (LD50/30) without any medical intervention. Therefore, the timely assessment of absorbed radiation dose is critical for saving human lives. Furthermore, estimating absorbed radiation dose assumes even greater importance in the case of large-scale accidents, where prioritizing the exposed population aids in the effective utilization of available medical resources.

In addition, DNA is a highly radiation-sensitive molecule. This molecule contains information to encode all proteins in the organism, and alterations in this molecule can be fatal. Both radiation itself and the free radicals generated by radiation cause adverse effects on DNA [4]: disruption of the nitrogenous bases (scission, modification or dimerization of nitrogen bases) and DNA strand breakage (which can occur on a single strand or on both strands). In some cases, damage to double-stranded DNA can be reflected at the chromosomal level. The cellular machinery has mechanisms to counteract such DNA damage to ensure the correct transmission of genetic information to daughter cells [5]. However, it may sometimes fail.

If two chromosomes fragment because of ionizing radiation at some point prior to replication, ideally, the repair mechanisms fuse each fragment with its corresponding chromosome. However, if both chromosomes are in close proximity to each other, a failure in the repair process can also occur and the fragments do not fuse with their original chromosome; instead, the fragmented chromosomes fuse with each other, and the fragments join together. This results in two types of chromosomes: those derived from the union of fragmented chromosomes, with two centromeres (dicentric chromosomes), and those derived from the fusion of fragments, without centromeres (acentric chromosomes).

Moreover, radiation damage to genetic material—when exposure exceeds the capacity of genetic repair mechanisms—has clear biological effects on cells. The mutation of certain genes alters proteins involved in the regulation of the cell cycle. These genes include oncogenes (genes that code for proteins that induce the cell cycle) and tumour suppressor genes (genes that code for proteins that inhibit the cell cycle) [6,7]. While mutations in oncogenes usually result in the overexpression of their products, mutations in tumour suppressor genes typically result in the deficient or absent expression of their products. In short, the alteration of oncogenes and tumour suppressor genes affects cell cycle progression and can lead cells to divide uncontrollably, i.e., cancer cells.

The appearance of cancer cells cannot be determined from the amount of radiation absorbed, as it depends largely on which genes are affected and the level of damage. Rather, the probability of their occurrence can be estimated; that is why they are known as stochastic effects. However, when a certain radiation threshold is reached, cell death by mitotic catastrophe occurs in any case. The DNA is so damaged that the checkpoints fail to stop the cell cycle and the cell goes into mitosis. To avoid the consequences of passing on aberrant genetic material to descendant cells, the cell enters either a state of senescence (permanent and irreversible cessation of the cell cycle and function) or undergoes cell suicide (apoptosis). When radiation causes cell death in tissues, damage occurs after a well-defined dose threshold. This non-probabilistic damage is called deterministic or non-stochastic damage.

Biological effects (acute or chronic) do not appear instantaneously. For this reason, the early detection of whether an individual has received radiation can be decisive for their survival (as long as treatment can be provided to mitigate the effects). This is the origin of biological dosimetry, which includes a set of techniques that make it possible to determine whether an individual has been exposed to IR and, if so, to quantify the absorbed dose. To predict health effects, evaluate risks and provide protection against ionizing radiation, various biological techniques are used, each with its own specific purpose:

1. Chromosome banding: This technique is used for chronic or acute exposures in a delayed manner. It consists of analyzing stable alterations in the chromosomes, providing information about the dose received.
2. FISH (fluorescence in situ hybridization): Also used in chronic or acute exposures, FISH can detect specific chromosomal abnormalities, such as translocations. It is useful for evaluating the cumulative dose over time.
3. Analysis of dicentric chromosomes: This technique is applied in acute exposures. Dicentrics are abnormal chromosomes that form after exposure to ionizing radiation. Their presence indicates a high radiation dose.
4. Analysis of binucleated or micronucleated cells: Another technique for acute exposures. Micronucleus cell counting provides information on the dose received and is used in emergency situations.

How can we measure the absorbed radiation dose in humans in a minimally invasive manner? The ubiquitous nature of circulating blood lymphocytes and their inherent radiosensitivity make them an ideal model system for estimating the absorbed radiation dose in humans. Bender and Gooch [8,9] first demonstrated the utility of the Dicentric Chromosome Assay (DCA) for estimating the absorbed dose (biodose) in individuals exposed during the Recuplex criticality accident in Hanford, WA, USA. These seminal studies laid the foundation for cytogenetics-based biodosimetry and, since then, numerous studies have utilized DCA for absorbed radiation dose estimation in the victims of Chernobyl [10–13] and Fukushima Daiichi. Since most deterministic effects increase as a function of radiation dose, absorbed dose estimation will help in choosing the appropriate medical countermeasures to mitigate or alleviate the severity of IR-induced radiation injuries or sickness.

The DCA is universally accepted as the gold standard for absorbed radiation dose estimation [14] due to several salient features: (I) the low baseline frequency of dicentric chromosomes (1 dicentric chromosome in 1000 T-lymphocytes, 0.001/cell), (II) baseline frequency is not modulated by age and gender, (III) it is fairly specific to radiation exposure, (IV) it has a radiation dose-dependent formation and (V) the detection range is from 0.05 to 5 Gy. The upper limit of detection can be extended to >20 Gy using a technique known as prematurely condensed chromosomes (PCCs), performed by cell fusion in the G0/G1 phase and by Calyculin-A in the G2 phase of the cell cycle. Since the centromeric regions of the PCCs are not clearly detectable in Giemsa-stained preparations, fluorescence in situ hybridization (FISH) with a pan-centromeric DNA probe is needed to detect dicentric chromosomes. Dicentric chromosomes are formed due to the mis-rejoining of two broken chromosomes with intact centromeres. Dicentric chromosomes, in most cases, are

accompanied by acentric fragments resulting from the two broken chromosomes. Since the number of dicentric chromosomes increases as a function of radiation dose, absorbed radiation dose can be easily estimated from the frequency of dicentric chromosomes using several currently available algorithms (Dose Estimate, CABAS and BioDose) with an ex vivo generated dose–response curve, using either X-rays or gamma rays.

DCA is labor-intensive and the turnaround time for dose estimation varies from 72 to 96 h. Manual scoring of dicentric chromosomes creates one of the bottlenecks for large-scale incidents or accidents where absorbed dose estimation is needed for hundreds of thousands of exposed individuals. Developing an efficient automated detection system for dicentric chromosomes would considerably shorten the manual scoring time and help in biodose estimation for medical intervention, particularly for those who received high-dose exposures (>2 Gy).

To accelerate the speed of dicentric chromosome detection/counting in the metaphase images of lymphocytes, an AI-based approach was undertaken in this study. Studies have shown that there is a relationship between the frequency of dicentric chromosomes and radiation esposure dose [15–17]. The frequency ofdicentrics is dependent on the absorbed dose. The linear quadratic equation for the yield of dicentrics is as follows:

$$Y = \alpha D + \beta D^2 + c$$

where Y corresponds to the frequency of dicentrics, D to the radiation dose and c to the frequency of dicentrics prior to exposure. α and β are coefficients obtained from statistical analysis. Owing to a low base line frequency of dicentric chromosomes in healthy individuals (1 dicentric chromosomes in 1000 lymphocytes 0.001/cell), the c value is usually negligible [18]. On the other hand, the coefficient β usually tends toward 0 for particularly high LET radiation such as neutrons. Hence, in this way, the dose effect relationship is linear for dicentrics:

$$Y = \alpha D$$

Therefore, the absorbed radiation dose can be easily estimated from the yield of dicentric chromosomes, and thus the prognosis of the patient can be established: an individual who has received an absorbed dose less than 2 Gy has a high chance of survival; if the absorbed dose ranges between 2 and 6 Gy, there is a chance of survival if the individual receives adequate medical countermeasures; and if the absorbed dose is higher than 6 Gy, chance of survival will be minimal, and therefore palliative treatment should be given.

Initial approaches on the automation of dicentric chromosomes focused on segmentation techniques [19,20], whereas more recent studies have achieved high precision and accuracy levels using convolutional neural networks [14,21–23].

The aim of this work is to identify dicentric chromosomes in the images of metaphase cells by developing an artificial intelligence software based on deep learning and computer vision for distinguishing between damaged (dicentric chromosomes) and undamaged chromosomes (monocentric). Specifically, an ensemble of detectors is proposed in this work. An ensemble aims to merge the results of the models that compose it, and this strategy has been widely used in earlier studies [24–27]. The decision made by consensus is likely to be more accurate than decisions made by individual models, since the consensus function used by the ensemble can correct some classification errors, provided the results from the individual models are accurate.

The remainder of this paper is organized as follows. Section 2 describes the methodology proposed in this work. Then, the experiments that have been carried out are described in Section 3. Finally, Section 4 details the conclusions of this work.

2. Methodology

The following section details our methodology for dicentric chromosome detection. Briefly, the detection system was divided into different steps. Figure 1 depicts a scheme of the entire detection process. An image of chromosomes in individual metaphase cells was

first supplied as an input to the system. Then, the image was preprocessed by applying different binarization operations and morphological filters separately. In this way, several distinct images were generated from the original one in this phase. After that, each generated image was transferred to a trained deep neural network. Once the predictions of all generated images were released by each model, they were combined using a consensus function to produce the final output prediction.

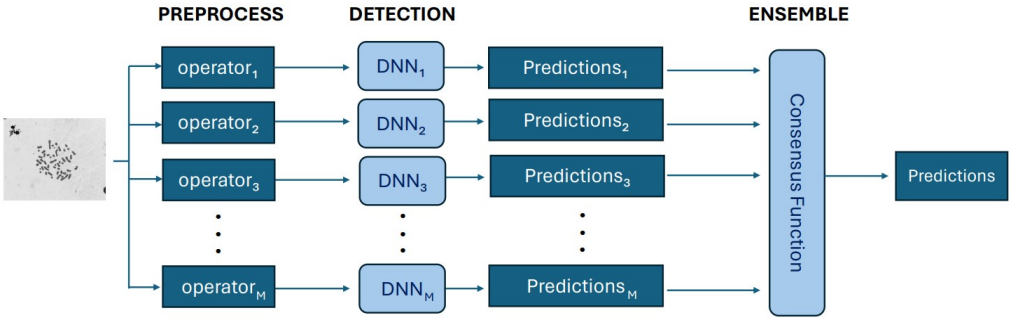

Figure 1. Schema of the overall proposal's operation. The input image is preprocessed using multiple operators. Each preprocessed image is supplied independently on a deep neural network (DNN) model. Predictions released by each model are finally merged by ensembling and evaluated with a consensus function, producing the final output prediction .

2.1. Image Processing Operators

First of all, let us denote $\mathcal{S}$ as a set of input patterns for dicentric chromosome detection containing N patterns, where the i-th training pattern is composed of a raw image $\mathbf{X}_i$ and its corresponding exact ground-truth $\mathbf{y}_i$ where the target objects were chromosomes (dicentric and non-dicentric (also known as monocentric)):

$$\mathcal{S} = \{(\mathbf{X}_i; \mathbf{y}_i) \mid i \in \{1, ..., N\}\} \tag{1}$$

Now, let us assume that an image processing operator G_j, $j \in \{1, ..., M\}$ affects the images while the ground-truths remain unchanged, where M is the number of different operators considered, such as binarization or morphological filters. Therefore, the j-th operator takes the image $\mathbf{X}_i$ as input and produces the processed image $\tilde{\mathbf{X}}_{i,j}$.

$$\tilde{\mathbf{X}}_{i,j} = G_j(\mathbf{X}_i) \tag{2}$$

For the sake of notational simplicity, it will be assumed that $j = 1$ corresponds to the no-operation operator, i.e., $\tilde{\mathbf{X}}_{i,1} = \mathbf{X}_i$.

Then, we may denote $\mathcal{T}$ as the training set for dicentric chromosome detecting, which is made of $N \times M$ training patterns:

$$\mathcal{T} = \left\{ \left(\tilde{\mathbf{X}}_{i,j}; \mathbf{y}_i\right) \mid i \in \{1, ..., N\}, j \in \{1, ..., M\} \right\} \tag{3}$$

2.2. Chromosome Detection by Neural Network

The second stage consists of M deep convolutional neural networks, denoted as $\mathcal{D}_j$, $j \in \{1, ..., M\}$, for object detection. The model $\mathcal{D}_j$ is generated after a training process by using those images from $\mathcal{T}$ obtained by the operator G_j and their associated ground-truth. A YOLOv8 model [28] has been used as the selected neural network architecture. The application of this model is not limited to the proposed approach and can be replaced with other object detection models if needed.

Each neural network receives an image $\mathbf{Z}$ as input and produces a set of detections (detected chromosomes) $\mathcal{R}$ as output.

$$\mathcal{R}_j = \mathcal{D}_j(\mathbf{Z}) \tag{4}$$

Each k-th detection $r_{j,k}$ contains an axis-aligned bounding box $\mathbf{w}_{j,k}$, an object class label $q_{j,k}$, and a confidence level $v_{j,k}$:

$$R_j = \left\{ r_{j,k} \mid k \in \{1, ..., W\} \right\} \tag{5}$$

$$r_{j,k} = \left(\mathbf{w}_{j,k}, q_{j,k}, v_{j,k} \right), \; k \in \{1, ..., W\} \tag{6}$$

$$\mathbf{w}_{j,k} = \left(a_{j,k}, b_{j,k}, c_{j,k}, d_{j,k} \right) \tag{7}$$

where W is the number of detections, $\left(a_{j,k}, b_{j,k} \right) \in \mathbb{R}^2$ are the coordinates of the upper left corner of the k-th detection within the image $\mathbf{X}$, $\left(c_{j,k}, d_{j,k} \right) \in \mathbb{R}^2$ are the coordinates of the lower right corner of the k-th detection within $\mathbf{X}$, $q_{j,k}$ is the class label of the k-th detection, and $v_{j,k} \in \mathbb{R}$ is the confidence level of the k-th detection.

A minimum confidence level v_{min} is defined so that detections below that threshold are ignored. As a result, the filtered set of detections is computed:

$$R'_j = \{ r_{j,k} \in R_j \mid v_{j,k} \geq v_{min} \} \tag{8}$$

2.3. Ensemble of Networks

Next, an ensemble of detector networks framework is described. This ensemble is proposed to enhance the classification performance of the individual networks presented before. The aim of the ensemble is to merge the results of the previously considered networks. This is because a decision made by consensus is generally more accurate than decisions made by individual networks. The reason for this is that the consensus process can correct some classification errors, provided that the majority of the outputs from the individual networks are accurate. It is expected that the more diverse the operators G_j are, the more likely that the ensemble will provide better outcomes than any of its members.

Then, the consensus strategy to combine the results coming from the elements of the ensemble to yield the proposed consensus output is computed as follows:

$$R'_\varphi = \varphi\left(\left\{ R'_j \mid j \in \{1, ..., M\} \right\} \right) \tag{9}$$

where φ is a suitable aggregation function.

3. Experimental Results

This section describes the dataset used in the experiments, the preprocessing methods selected, and the results obtained.

3.1. Dataset

This study used a private set of chromosome micrographs provided by Dr. Adayabalam S. Balajee from the *Radiation Emergency Assistance/Training Site (REAC/TS)* of the *Oak Ridge Institute for Science and Education* (ORISE) in Tennessee, USA, and by Dr. Alegría Montoro Pastor from Hospital La Fe, Valencia, Spain. The dataset included 50 images of metaphase cells that were prepared from 2 Gy irradiated lymphocytes ex vivo. Chromosomes were stained using the Giemsa technique, and the image size ranged from 732 pixels to 1024 pixels in height and from 912 pixels to 1280 pixels in width. The images include a total of 2339 chromosomes, of which 87 are dicentric (3.72%). Some images from the dataset used in the study are provided in Figure 2. In these images, normal chromosomes (monocentric) and damaged chromosomes (dicentrics—chromosomes with two centromeres) can be observed.

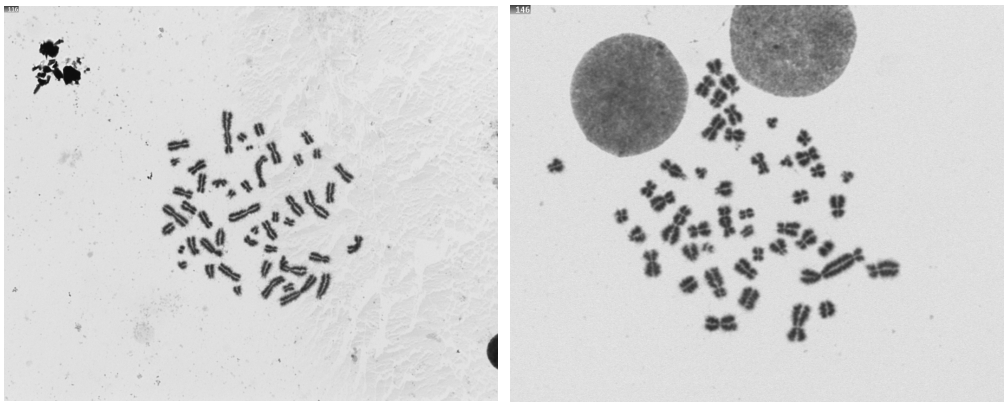

Figure 2. Example of two images from the dataset, where normal chromosomes and chromosomes with two centromeres (dicentric) are presented.

3.2. Preprocessing

In preprocessing, the images were converted to grayscale, binarized, and then a morphological operation with a given filter size was applied. Two techniques were used for threshold selection: Otsu and Spline. The Otsu technique [29] uses variance to find the threshold value that minimizes variance between pixels within the same segment and maximizes variance between pixels in different segments. The Spline technique uses data obtained from histograms of grayscale images to select the intensity of the largest peak generated by dark pixels.

The morphological filters used were opening and closing filters, which sequentially apply erosion and dilation (opening filter) or dilation and erosion (closing filter). The erosion filter consists of converting all pixels in the image that are surrounded by a pixel with a white value to white. The dilation filter consists of converting all pixels in the image that are surrounded in any of their eight neighboring pixels by a pixel with a white value to black, while the dilation filter consists of converting all pixels in the image that are surrounded in any of their eight neighboring pixels by a pixel with a black value to black. Additionally, different filter sizes were used: 2×2, 3×3, 4×4, 5×5.

3.2.1. Binarization and Thresholding Techniques

For the selection of the threshold value, two different techniques have been employed, one of our own devising and another applied in a paper also focused on the detection of dicentric chromosomes through a two-stage convolutional network that uses a single type of image preprocessing [14].

Our process consisted of obtaining image histograms (plots showing the number of pixels present for each intensity value) and plotting a representative polynomial (hereafter a Spline curve) of the discrete set of points through interpolation. On this curve, the points representing local maxima were identified. To determine the threshold value for the binarization process, the chosen value was selected from the valley between the peaks. (see Figure 3). To fix the values for the binarization parameters with the methods Spline and Otsu, samples from the first split (only ten images) of the dataset were selected.

When we observed that one of the selected images exhibited three peaks (local maxima), unlike most images with two peaks, we carefully analyzed the whole dataset for our own research interest and found that only two cases from the whole dataset (50 images) displayed three peaks. In 48 cases, two thresholds appear: the first from the black peak (which corresponds to the chromosomes), and the second from the white peak (which corresponds to the background). Binarization was performed using the threshold derived from the black peak. Only two cases in the whole dataset (images 2Gy-068 and 2Gy-360) showed three local maxima, and therefore three thresholds observed (see Figure 4). In both cases, two of these thresholds corresponded to black peaks, and only the binarization using the threshold generated from the largest black peak (i.e., the peak with the largest

number of pixels) produced acceptable results (recognizable chromosomes), regardless of whether the lower black peak was to the left or right of the upper black peak. Taking this into account, the threshold selection was the one generated by the maximum of the peaks, excluding the last peak (which is always higher in the number of pixels since it corresponds to the background).

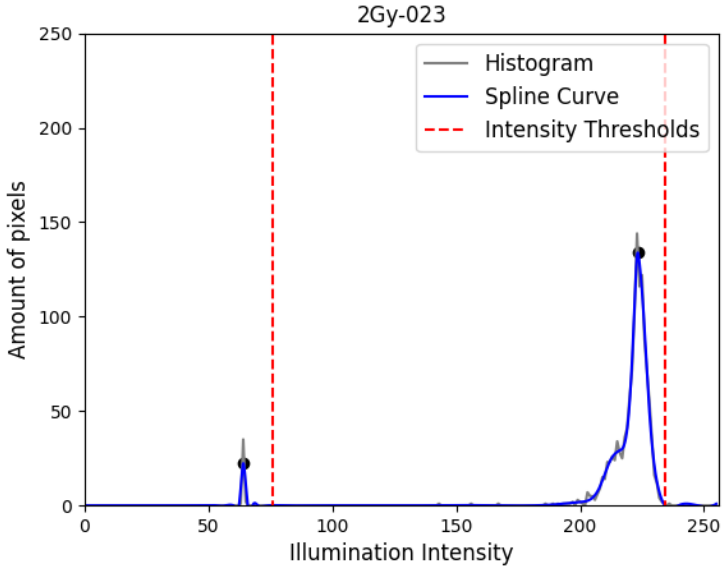

Figure 3. Histogram of image 2Gy-023 with Spline curve and thresholds obtained from local maxima (black peak on the **left** and white peak on the **right**).

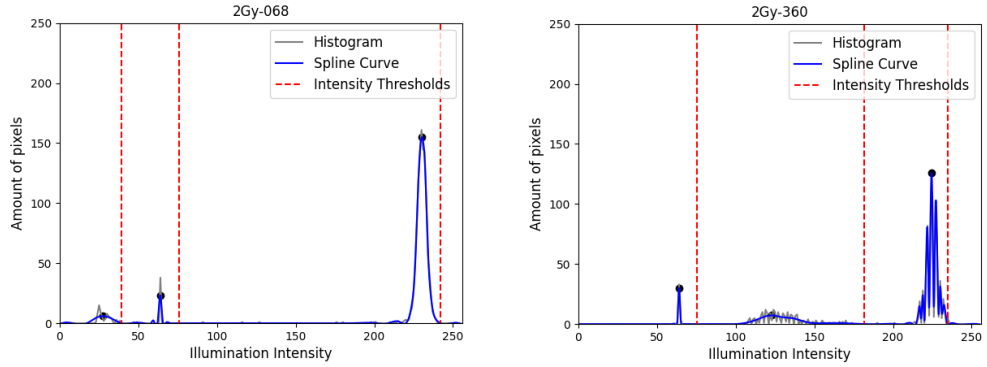

Figure 4. Histogram of images 2Gy-068 and 2Gy-360 with Spline curve and thresholds obtained from local maxima (black peak on the **left** and white peak on the **right**). Note that three peaks are presented.

Once binarization was applied, it was observed that, although in most chromosomes, the thresholding allowed perfect recognition and even to distinguish between dicentric and non-dicentric chromosomes, the threshold was significantly displaced to the left in some images, rendering these images unsuitable for training the model (even though the threshold is obtained when a valley of the histogram is reached).

On the other hand, the results obtained from thresholding with Otsu's method (used in the previously mentioned study [14]) were studied, while using Otsu's algorithm to set the threshold solves the problem that arose when using the Spline technique alone. It should be noted that the separation between sister chromatids is small—zero in many of the chromosomes—and that this could be an obstacle to the model in discerning between dicentric and non-dicentric chromosomes. A comparison between the methods is presented in the first row of Figure 5.

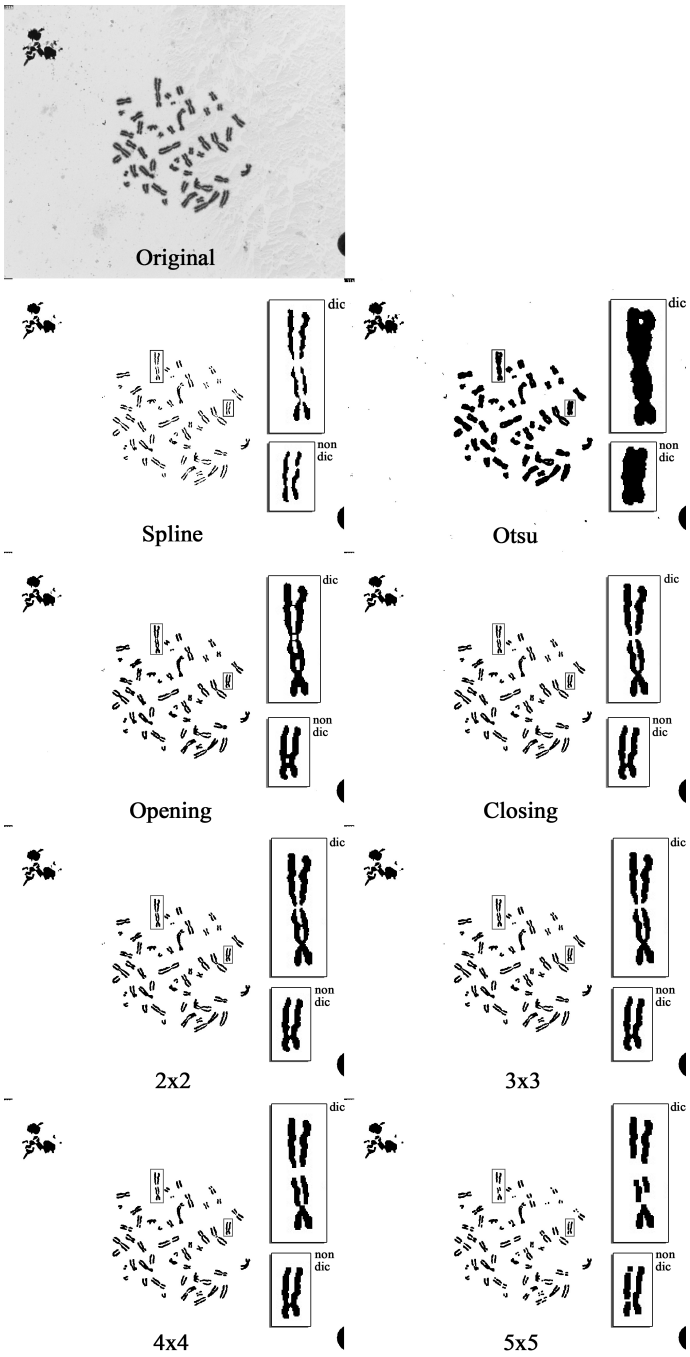

Figure 5. Preprocessing techniques applied on example image. First row: original image. Second row: comparison between filter sizes for image 2Gy-023. In this example, the thresholding technique (Spline) and the type of morphological filter (closing) have been kept constant. Third row: comparison between opening and closing morphological filters for image 2Gy-023. In this example, the thresholding technique (Spline) and the filter size (3×3) were kept constant. Fourth and fifth rows: comparison between filter sizes for image 2Gy-023. In this example, the thresholding technique (Spline) and the type of morphological filter (closing) have been kept constant.

3.2.2. Morphological Filters

The erosion filter consists of converting all the pixels of the image that are surrounded, in any of their eight neighboring pixels, by a pixel with a white value to white. On the other hand, the dilation filter consists of turning all the pixels of the image that are surrounded, in any of its eight neighboring pixels, by a pixel with a black value to black.

In addition, the opening filter consisted of the sequential application of an erosion filter and a dilation filter (in this order), while the closing filter consisted of the sequential application of a dilation filter and an erosion filter (in this order). While the opening filter was used to remove protruding elements, the closing filter was used to join elements separated by a narrow gap.

On the other hand, the size chosen for these filters will eventually determine the proportion to which the image will be affected. In this experiment, opening and closing filters with filter sizes of 2×2, 3×3, 4×4 and 5×5 were applied and each combination was studied separately.

After applying binarization, it was observed that in some chromosomes, gaps in the pixels had higher gray values when viewed in grayscale. In particular, this occurrence around the centromeres as well as the ends of the chromosomes (telomeres) could be problematic, since it might miss one of the centromeres of a dicentric chromosome, resulting in the erroneous interpretation of a dicentric chromosome as a false negative. In such scenarios, the opening filter proved to be useful by recovering the bonds between sister chromatids. However, in other cases, the opening filter caused the appearance of closing points between chromatids that are not real centromeres and could therefore be interpreted as a false positive by the model.

On the other hand, the closing filter worked optimally in the opening of non-centromeric regions between sister chromatids that appeared as a product of binarization. However, in other cases, it removed centromeres from the chromosomes and could lead to the interpretation of false negatives by the model (see second row of Figure 5).

With respect to filter size, the use of 2×2 size filters introduced very few noticeable changes in the images, while 5×5 size filters greatly distorted the chromosomes. The 3×3 and 4×4 filters introduced changes that varied between the two extremes (see fourth and fifth rows of Figure 5).

As can be seen, each of the configurations introduced a number of advantages and disadvantages depending on the image quality and variations in chromosome morphology.

3.3. Results

A 5-fold cross validation was applied on every experiment to ensure that training and validation partitions were independent of each other and that the training was not biased. To this end, the dataset, which was randomly reordered, was split into five partitions. Since the dataset is composed of 50 images (see Section 3.1 for more details), each partition is formed by 10 images. Thus, each deep neural network model used one split for validation (10 images) and the remaining partitions for training (40 images).

The model used in this study was the YOLOv8x neural network, which consists of a structure of 640 pixels and 68.2 million parameters [28]. The YOLO architecture is based on a feature pyramid neural network consisting of multiple layers that detect objects at different scales. This pyramid consists of two main parts: the head, responsible for launching the predictions, and the backbone, which improves the information flow between the different layers of the network. Both parts use a module called C2f (cross-stage partial bottleneck with two convolutions), which merges contextual information with high-level features to enhance detection performance [30,31]. The model was trained using pre-trained weights from common object detection. As previously mentioned in Section 2, the use of this model is not limited to the proposed approach and can be modified for use with other object detection models if desired. To avoid a high number of false positives, only predictions with confidence and intersection over union values of at least 0.7 were selected (i.e., $v_{min} = 0.7$). Regarding the augmentation algorithms used in the training processing, the YOLO algorithm automatically applies multiple data augmentation techniques by default. The algorithms included hue adjustments, modification of saturation and brightness values, image rotations, vertical and horizontal image flips, image scaling, image shearing from different angles, perspective transformation, vertical and horizontal image translation, channel shifting (from RGB to BGR), the compositing of several images

into mosaic, the deletion of parts of the image, and image fraction crop. The remaining parameters of YOLO were kept at default values. Table 1 exhibits more detail about the parameters and the tuned values.

Table 1. Tuned configurations for the parameters of the proposal.

Parameter	Description
v_{min}	Minimum confidence threshold for detections. The detector disregards those objects detected with a confidence below this threshold. The parameter is noted as $conf$ in YOLOv8x (default value of 0.25). In this work, $v_{min} = 0.7$.
iou_detector	Intersection Over Union (IoU) threshold for Non-Maximum Suppression (NMS). Parameter used by YOLOv8x noted as *iou* with a default value of 0.7.
ϕ	The aggregation function of the ensemble. In this work, it combines the prediction provided by the different methods of which the ensemble is composed. That combination disregards those objects with an IoU below the *iou_ensemble* threshold and those predictions with at least a certain percentage of coincidence between the ensemble's members (*quota*).
iou_ensemble	IoU threshold for consensus merged prediction. The ensemble disregards those merged objects detected with IoU below this threshold. In this work, $iou\_ensemble = 0.5$.
quota	The ensemble disregards those merged objects detected if the percentage of coincidence between the ensemble's members is below this threshold. In this work, $quota = \{0.05, 0.1, 0.2, 0.3, 0.40.5\}$.

As mentioned in Section 2, the use of the YOLOv8x detector is not confined to the proposed methodology and can be substituted with other detector models if required. In this work, the YOLOv8x neural network was chosen after a preliminary performance comparison between different YOLOv8 versions, such as YOLOv8n or YOLOv8m. Other detectors, such as Faster-RCNN ResNet or MobileNet models, were discarded because their detection performances, in general, are similar to those yielded by YOLOv8 models, and their computational times are considerably longer [32]. The considered initial models (YOLOv8 versions) were trained over the raw image dataset, and their achieved performances related to the accurate detection of dicentric chromosomes were analyzed. Since dicentric chromosome detection involves evaluating medical images, the computational execution time is not crucial in terms of real time. Therefore, this measure was omitted in our comparison. As expected, YOLOv8x achieved the highest scores in that preliminary comparison. Thus, YOLOv8x was selected as the architecture detector to compose the ensemble proposed in our methodology.

The possible combinations of the thresholding technique used in binarization (Spline or Otsu), the morphological filter type (opening or closing), and the filter size (2×2, 3×3, 4×4 and 5×5) constituted the configurations with which each model was trained.

Regarding the consensus function, it combines the prediction provided by the different methods that compose the ensemble. In this work, that combination was considered to be the merging of the detections with an iou value higher than 0.50. After that, only those detections with at least a certain percentage of coincidence between the ensemble's members were considered. Therefore, if a prediction was not provided by a certain percentage of the ensemble's members, that prediction was filtered out and not used within the prediction provided by the ensemble. In this way, the aggregation function ϕ, which defines the consensus strategy used in these experiments, is a combination of the predictions provided by the ensemble methods where the detection prediction is filtered if a minimum percentage of coincidence between the ensemble's members is not surpassed. That minimum percentage of coincidence between the ensemble's members is noted as *quota*. In this way, for example, "Consensus 0.10" returns a detection prediction if at least 10% of the members detect it. Respecting the consensus classification prediction for a given predicted detection, it is computed as the average of the classification predictions for that detection. The detections to be merged were those provided by each combination of binarization technique (Otsu

and Spline), morphological operator (opening and closing filters) and size of filter (2×2, 3×3, 4×4, and 5×5). Respecting the percentage of coincidence between the ensemble's members, different values were tested: 0.05, 0.1, 0.2, 0.3, 0.4, and 0.5.

It must be emphasized that the balance between complexity and accuracy must be managed critically when an ensemble strategy is proposed. Generally, the higher the number of networks in the ensemble, the better the system's detection performance, while a lower number of networks leads to a faster system. However, the optimal number of networks in an ensemble may vary greatly depending on different factors. For example, the specific problem to be addressed is crucial for determining which kind of system will be suitable: a sensitive issue (for example, evaluating medical images) may require the highest possible detection performance, while a real-time problem (for example, estimating traffic flow from road video sequences) may require a fast output. In our work, to achieve the highest possible detection performance, we considered a high number of networks within the ensemble. This number is the result of each combination of binarization technique (Otsu and Spline (i.e., two possibilities)), morphological operator (opening and closing filters (two possibilities)) and size of filter (2×2, 3×3, 4×4, and 5×5 (four possibilities)), plus the non-operation model, resulting in an ensemble composed of 17 networks (thus, M = 17).

It has been observed that, for most subdivisions of the dataset from all the methods, the loss function tends to decrease over epochs (see Figure 6) for both the detection and classification of chromosomes into dicentric or non-dicentric. This behaviour occurs in both the training and validation processes, so the model does not exhibit overfitting characteristics. Likewise, it is also noteworthy that the precision, completeness and mAP50 functions tend to grow over epochs, which is a remarkable aspect of the model performance. However, it should be noted that the values reached in the last epoch are not always as high as desired. It is interesting to observe how the evaluation curve of the mAP50 indicator shows abnormal fluctuations. The reason for this is that the dataset exhibits a strongly unbalanced class distribution besides a high variance in object sizes, a low number of samples, and low-resolution images. These facts raised difficulties in accurately classifying dicentric chromosomes, impacting the evaluation metric throughout the training. An example of the predictions is shown in Figure 7. As illustrated, all the chromosomes are well detected, but not well classified.

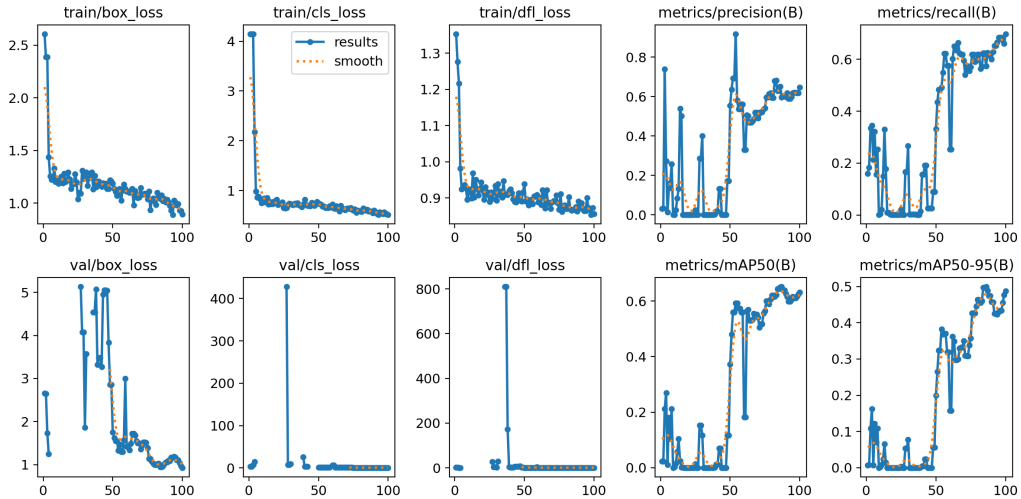

Figure 6. Model performance for the 2×2 Spline closing method. It can be noted that loss function decreases over the epochs, whereas the recall, precision and mAP50 metrics increase.

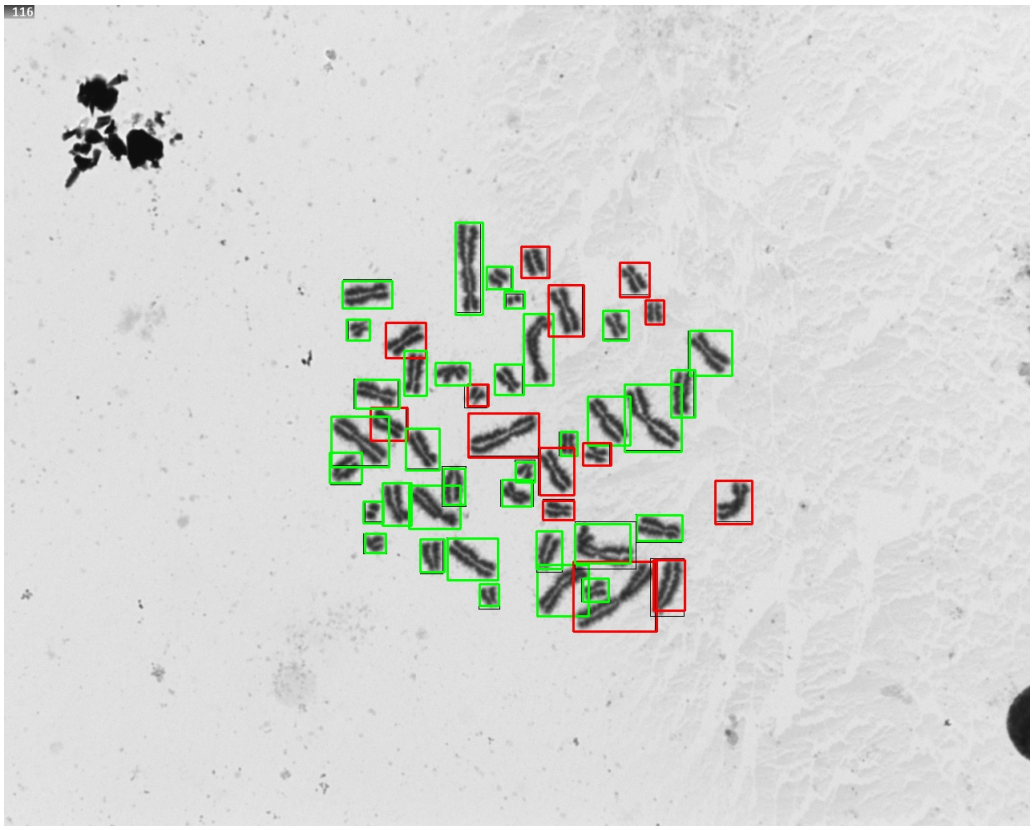

Figure 7. Prediction for the chromosomes of the image 2Gy-329 for the experiment where the Spline thresholding technique with 2 × 2 closing filter was employed. In green: predictions as 'non-dicentric'; in red: predictions as 'dicentric'.

From a qualitative point of view, it could be stated that the models, in general, have not presented problems in the detection of chromosomes and the predictions showed a high correspondence with the bounding boxes of the ground truth. As far as classification is concerned, each experiment showed better or worse results depending on the image being examined. Figures 8 and 9 compare their performance in the recognition of a dicentric (anomalous) chromosome and a non-dicentric (non-anomalous, or normal) chromosome, respectively. In Figure 8, it can be seen that a specific dicentric chromosome is detected and classified as dicentric in most experiments. Figure 9 shows a monocentric chromosome that was detected and classified as undamaged in most experiments.

The results achieved by our methodology have been interpreted in two phases: detection and classification. A schematic diagram is given in Figure 10.

In the detection phase, we analyzed whether the chromosomes were detected by the model regardless of their class. To consider that a chromosome has been detected, a condition was imposed requiring a prediction with an IoU (Intersection over Union) greater than 0.7. Subsequently, analysis of the count of detected chromosomes (true positives), undetected chromosomes (false negatives) and uncorrelated predictions (false positives) was carried out.

In the classification phase, we studied whether the chromosomes detected were correctly classified by the model. Four cases were recorded: anomalous chromosomes predicted as such (true positives), non-anomalous chromosomes predicted as such (true negatives), anomalous chromosomes predicted as non-anomalous chromosomes (false negatives) and non-anomalous chromosomes predicted as anomalous chromosomes (false positives).

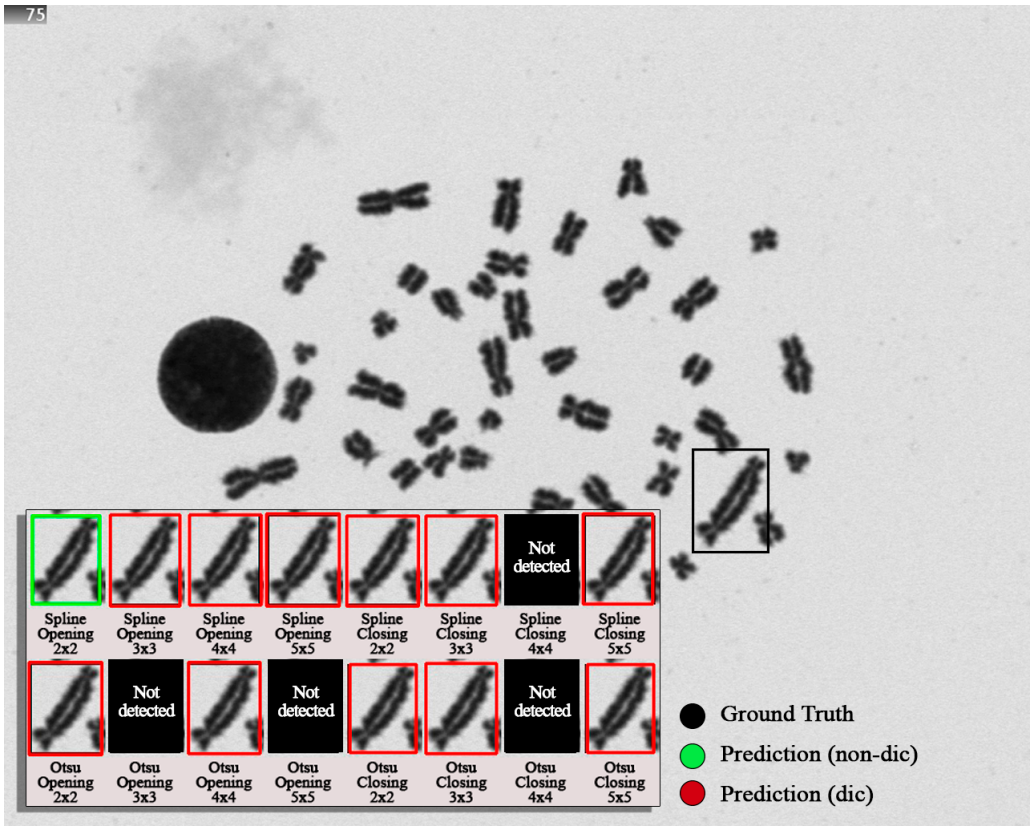

Figure 8. Composition of 2Gy-329 image predictions for a dicentric chromosome. In green: predictions as 'non-dicentric'; in red: predictions as 'dicentric'.

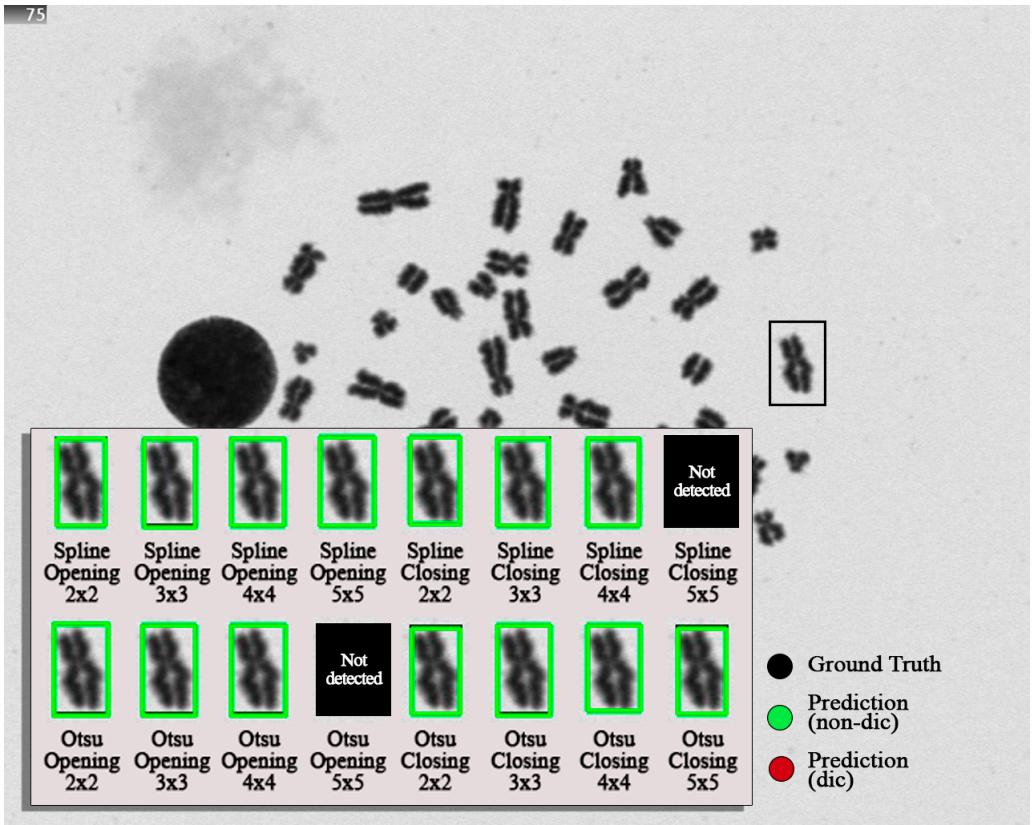

Figure 9. Composition of 2Gy-329 image predictions for a non-dicentric chromosome. In green: predictions as 'non-dicentric'; in red: predictions as 'dicentric'.

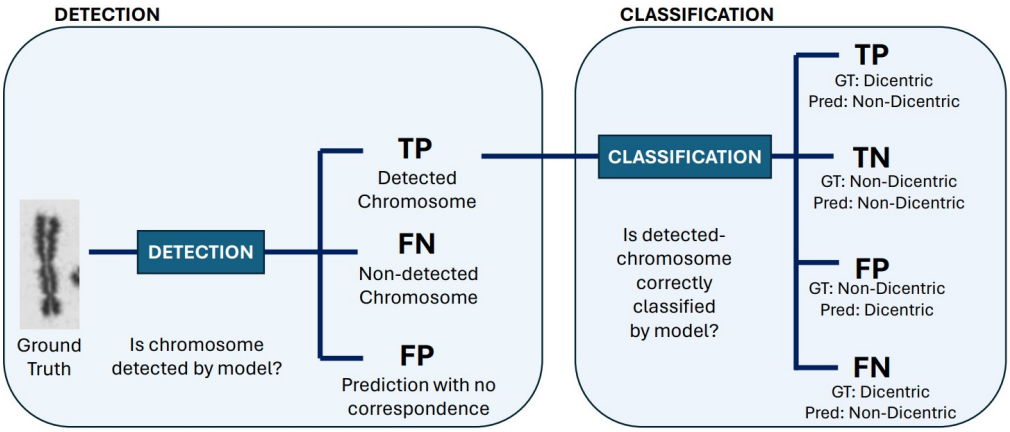

Figure 10. Schema of the ensemble operation. In a first phase, it is shown whether each ground truth chromosome is detected by the model. Then, in a second phase, for those chromosomes that were detected, it is shown whether the model classifies correctly as dicentric or non-dicentric.

Subsequently, a data assembly (ensemble) was performed to evaluate the results obtained and to determine a consensus function that will enhance the overall performance.

To establish a fair comparison between the tested models, different well-known metrics were selected. In this study, spatial accuracy (S), accuracy (Acc) and F-measures (Fm) were considered. These metrics provide an overall view of the model performance and return values between 0 and 1 (higher values are better). Their definitions are as follows:

$$\mathrm{Fm} = 2\frac{PR * RC}{PR + RC} \qquad S = \frac{TP}{TP + FN + FP} \qquad Acc = \frac{TP + TN}{TP + FP + FN + TN} \tag{10}$$

$$RC = \frac{TP}{TP + FN} \qquad PR = \frac{TP}{TP + FP} \tag{11}$$

From these measures, the performance of the proposal was studied for each of the methods and the results are shown in Tables 2 and 3. In particular, Table 2 reports the detection performance of all considered methods, while Table 3 shows their classification performance. In both tables, the different methods considered in this work can be organized into three groups: no operation method (the baseline), methods that combine binarization and thresholding techniques, and consensus methods (that are composed of the methods from both the two previous groups).

Figure 11 summarizes the detection performance of the baseline method (no operation), the best methods for each combination of binarization technique and morphological filter (nc5, no2, sc2 and so3), and the best ensemble methods (consensus 0.1, 0.2 and 0.3). As shown, the performance of the baseline method is considerably higher than that of the remaining methods that belong to the ensemble (nc5, no2, sc2, and so3). Regarding the ensemble, it considers the prediction of each method independently and merges them by using the aggregation function. Although these other methods separately yield worse results than the baseline, the ensemble offers a more accurate response compared with the baseline.

Regarding chromosome detection, in general terms, it can be observed that the number of true positives is much higher than the number of false positives (unmatched predictions) and false negatives (undetected chromosomes), although these values are still significantly high. Spatial accuracy is quite high in most of the experiments, whereas F-measure seems to be better in those experiments that apply the opening morphological filter.

Table 2. Performance of the detection of chromosomes. The first column indicates the operator ('n' and 's' stand for Otsu and Spline techniques, respectively; 'c' and 'o' stand for closing and opening morphological filter, respectively; the value next to consensus means the minimum percentage of coincidence between the ensemble's members to be considered for each predicted detection) and the remaining columns show the yielded mean performance.

Method	TP	FP	FN	RC	PR	FM	S
No operation	2256	2	83	0.96	1.00	0.49	0.96
nc2	2004	227	335	0.86	0.90	0.44	0.78
nc3	2139	854	200	0.91	0.71	0.40	0.67
nc4	1976	700	363	0.84	0.74	0.39	0.65
nc5	2004	0	335	0.86	1.00	0.46	0.86
no2	2144	7	195	0.92	1.00	0.48	0.91
no3	2086	2	253	0.89	1.00	0.47	0.89
no4	2139	51	200	0.91	0.98	0.47	0.89
no5	1956	1987	383	0.84	0.50	0.31	0.45
sc2	1836	100	503	0.78	0.95	0.43	0.75
sc3	1693	271	646	0.72	0.86	0.39	0.65
sc4	1030	8	1309	0.44	0.99	0.31	0.44
sc5	799	1794	1540	0.34	0.31	0.16	0.19
so2	1804	210	535	0.77	0.90	0.41	0.71
so3	1887	51	452	0.81	0.97	0.44	0.79
so4	1791	186	548	0.77	0.91	0.41	0.71
so5	1808	1	531	0.77	1.00	0.44	0.77
Consensus 0.05	2330	6450	9	1.00	0.27	0.42	0.27
Consensus 0.1	2314	0	25	0.99	1.00	0.99	0.99
Consensus 0.2	2278	0	61	0.97	1.00	0.99	0.97
Consensus 0.3	2211	0	128	0.95	1.00	0.97	0.95
Consensus 0.4	2159	0	180	0.92	1.00	0.96	0.92
Consensus 0.5	2012	0	327	0.86	1.00	0.92	0.86

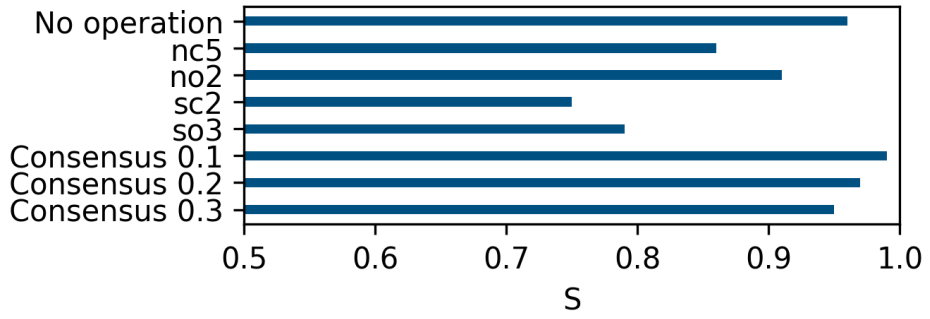

Figure 11. Detection performance (spatial accuracy) achieved by the baseline method (no operation), the best methods for each combination of binarization technique and morphological filter (nc5, no2, sc2 and so3), and the best ensemble methods (consensus 0.1, 0.2 and 0.3).

The performance of the experiment applying Otsu's 2×2 opening stands out from the rest, but falls short of the performance of the experiment applying no operator at all. However, when the ensemble of all operators is used, it outperforms the experiment that does not apply any operator. It must be highlighted that the performance yielded by the consensus respects that achieved by the detector applied directly over the raw images (the traditional and simplest strategy to face a detection problem), which corresponds with the "No operation" row. As reported for "Consensus 0.1" and "Consensus 0.2", both proposals outperform the "No operation" method.

Table 3. Performance of the classification of chromosomes. The first column indicates the operator ('n' and 's' stand for Otsu and Spline techniques, respectively; 'c' and 'o' stand for closing and opening morphological filter, respectively; the value next to consensus means the minimum percentage of coincidence between the ensemble's members to be considered for each predicted detection) and the remaining columns show the yielded mean performance.

Method	TP	TN	FP	FN	RC	PR	FM	S	ACC
No operation	26	2178	6	46	0.36	0.81	0.50	0.33	0.98
nc2	12	1936	8	48	0.20	0.60	0.30	0.18	0.97
nc3	11	2068	9	51	0.18	0.55	0.27	0.15	0.97
nc4	9	1871	39	57	0.14	0.19	0.16	0.09	0.95
nc5	12	1936	8	48	0.20	0.60	0.30	0.18	0.97
no2	14	2068	9	53	0.21	0.61	0.31	0.18	0.97
no3	14	2026	2	44	0.24	0.88	0.38	0.23	0.98
no4	14	2062	10	53	0.21	0.58	0.31	0.18	0.97
no5	10	1889	8	49	0.17	0.56	0.26	0.15	0.97
sc2	6	1778	4	48	0.11	0.60	0.19	0.10	0.97
sc3	5	1634	9	45	0.10	0.36	0.16	0.08	0.97
sc4	10	987	3	30	0.25	0.77	0.38	0.23	0.97
sc5	5	768	4	22	0.19	0.56	0.28	0.16	0.97
so2	8	1727	17	52	0.13	0.32	0.19	0.10	0.96
so3	9	1812	17	49	0.16	0.35	0.21	0.12	0.97
so4	9	1731	1	50	0.15	0.90	0.26	0.15	0.97
so5	11	1742	8	47	0.19	0.58	0.29	0.17	0.97
Consensus 0.05	35	2167	76	52	0.40	0.32	0.35	0.21	0.95
Consensus 0.1	25	2203	25	61	0.29	0.50	0.37	0.23	0.96
Consensus 0.2	16	2187	8	67	0.19	0.67	0.30	0.18	0.97
Consensus 0.3	11	2135	1	64	0.15	0.92	0.25	0.14	0.97
Consensus 0.4	6	2089	1	63	0.09	0.86	0.16	0.09	0.97
Consensus 0.5	5	1952	0	55	0.08	1.00	0.15	0.08	0.97

With respect to the classification task, the models yielded a greater number of true predictions than false predictions for the chromosomes that were detected, with a remarkable majority of predictions corresponding to true negatives (correctly classified non-dicentrics). However, it is notable that the models faced difficulties characterizing the dicentric chromosomes. For example, in Figure 12, a dicentric chromosome was classified incorrectly in most of the experiments. There are significantly more false negatives (dicentrics that were not classified as such) than true positives (correctly classified dicentrics) in all the experiments. This drawback is evident in the metrics of the classification phase, in which the values for spatial accuracy and F-measure are not high enough for any of the methods.

It must be highlighted that there is no method that surpasses the performance achieved by the no-operation operator. However, when the ensemble was used, a higher number of dicentric chromosomes was correctly classified. These results might be due to the reduced rate of dicentric chromosomes relative to undamaged monocentric chromosomes in the images. This is presumably a stumbling block for the approach in the task of extracting the patterns that allow the identification of dicentric chromosomes. Likewise, if the initial dataset had a larger volume of images or the images had a higher resolution, perhaps the model might have performed better in recognizing the patterns that allow the classification of dicentric chromosomes. It should also be noted that this task by itself is a challenge for health professionals in distinguishing a dicentric chromosome from a monocentric chromosome when the chromatids are simply superimposed, which will negatively influence the analysis and interpretation.

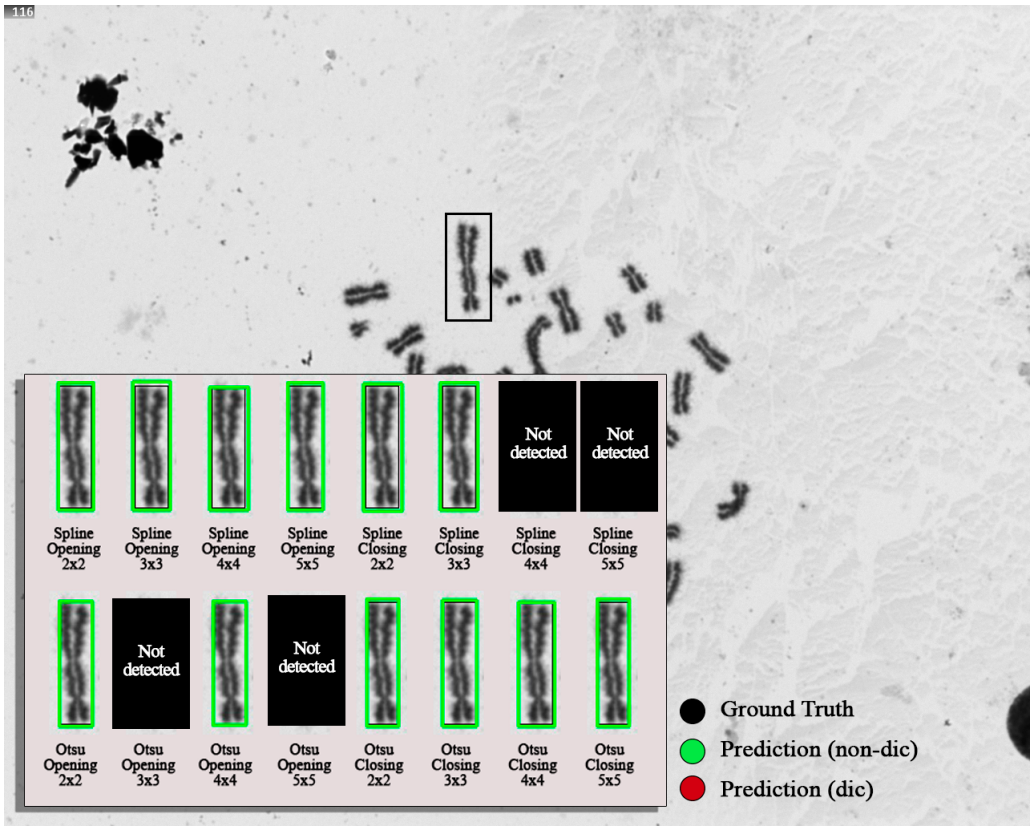

Figure 12. Composition of 2Gy-023 image predictions for a dicentric chromosome. In green: predictions as 'non-dicentric'; in red: predictions as 'dicentric'.

In contrast, no notable differences was observed in general terms between the performance presented by experiments that employed the Spline thresholding technique versus those that used the Otsu thresholding technique. In addition, it was also previously theorized that opening filters could lead to an increase in the number of false positives, while closing filters could lead to an increase in false negatives. It has been observed that, in the experiments that applied the Otsu thresholding technique, the number of false negatives was slightly higher in the experiments that applied closing filters versus those that applied opening filters, but no significant differences were observed in the number of false positives between opening and closing filters. Likewise, in experiments that applied the Spline thresholding technique, the number of false positives was slightly higher in experiments that applied opening filters versus those that applied closing filters, but no significant differences in the number of false negatives were observed between opening and closing filters.

Besides these obtained results and their analysis, it is remarkable that the dataset is highly challenging: it presents a low number of samples, a strongly imbalanced class distribution, a high variance in object sizes, and low-resolution images. In fact, several dicentric chromosomes from it are very difficult to detect, even by human experts in this field. Therefore, this sample size limitation offered by the dataset negatively affects the model's generalizability.

The main goal of this study was to develop an AI-based tool for the efficient detection of dicentric chromosomes which can expedite the dose estimation process and thereby enable a rapid triage. An automated analysis of dicentric chromosomes is expected to improve the dose prediction accuracy by avoiding variations in manual scoring between individual scorers. Additionally, AI-based tools can substantially advance the field of radiation biodosimetry in the development of predictive modeling for radiation induced early and delayed effects based on dose estimation. Future studies are required with

more images to fine-tune the AI tool for personalized medicine through dose estimation following incidental, accidental, occupational and intentional exposures.

4. Conclusions

The application of artificial intelligence techniques in the detection of dicentric chromosomes is a promising approach in the field of biological dosimetry, as AI-based tools have the capacity to improve the detection of dicentric chromosomes as well as the dose prediction accuracy when compared to laborious manual scoring. The automated detection of dicentric chromosomes can also drastically reduce inter-laboratory variations arising from discrepancies in dicentric chromosome scoring by laboratory personnel.

Our current work has focused on the use of convolutional neural networks to detect dicentric chromosomes in images of metaphase cells prepared from human lymphocytes. The images were preprocessed using different thresholding techniques, morphological filters, and filter sizes, and a model detector was trained for each of the selected operators. Then, we proceeded to apply data assembly techniques to enhance the performance of the model due to the low number of samples in the considered dataset. In this way, the same set of sample images was transformed into different datasets through several different transformations, and then different models were learned, which were finally evaluated by ensemble learning.

The performance, both in the process of chromosome detection and in the process of classification into dicentric or non-dicentric, was examined. Our study convincingly demonstrated that the approach applying the opening filters yielded significantly better results. The application of a detector over the raw dataset offers the best performance with respect to the individual performance achieved by each method; however, the use of an ensemble slightly surpasses that performance.

The dataset poses significant challenges due to its limited number of samples, highly imbalanced class distribution, considerable variance in object sizes, and low image resolution. In fact, several dicentric chromosomes within it are so difficult to detect that even human experts in the field struggle. Consequently, these sample size limitations negatively impact the model's generalizability.

Future experiments are needed for optimizing and developing AI-based tools to expedite the biodosimetry-based triage process for prioritizing medical treatments to save the lives of individuals exposed to high doses of IR. In particular, future research should aim to expand the dataset to include a more diverse range of samples, thereby enhancing the robustness and generalizability of the models. To achieve this, data augmentation techniques may be explored. Super-resolution, generating more detailed images, could also help to improve the detection and classification accuracies, besides exploring alternative neural network architectures and modern techniques, which could yield new insights.

Author Contributions: Conceptualization, M.J.R.-G., F.S.-P. and A.M.; methodology, M.A.M.-C.; software, I.A.-J.; validation, M.A.M.-C.; formal analysis, I.A.-J. and M.A.M.-C.; investigation, I.A.-J., A.S.B., M.J.R.-G., F.S.-P. and A.M.; resources, A.S.B., M.J.R.-G., F.S.-P., A.M. and M.A.M.-C.; data curation, A.S.B. and I.A.-J.; writing—original draft preparation, I.A.-J., A.S.B., M.J.R.-G., A.M. and M.A.M.-C.; writing—review and editing, I.A.-J., A.S.B., M.J.R.-G., F.S.-P., A.M. and M.A.M.-C.; visualization, I.A.-J.; supervision, M.A.M.-C.; project administration, M.J.R.-G. and M.A.M.-C.; funding acquisition, M.A.M.-C. All authors have read and agreed to the published version of the manuscript.

Funding: This work was partially supported by the Autonomous Government of Andalusia (Spain) under grant UMA20-FEDERJA-108, the Ministry of Science and Innovation of Spain under grant PID2022-136764OA-I00, the University of Málaga (Spain) under grants B4-2022, B1-2021_20 and B1-2022_14, and the Fundación Unicaja under grant PUNI-003_2023.

Data Availability Statement: The dataset used in this study is available on reasonable request from the corresponding author. The source code developed for this work is openly available https://github.com/icai-uma/Neural-networks-ensemble-to-detect-dicentric-chromosomes-in-metaphase-images (accessed on 10 November 2024).

Acknowledgments: The authors gratefully acknowledge the computer resources, technical expertise and assistance provided by the SCBI (Supercomputing and Bioinformatics) center of the University of Malaga. They also gratefully acknowledge the support of NVIDIA Corporation with the donation of a RTX A6000 GPU with 48 Gb. The authors also gratefully acknowledge the grant from the Universidad de Málaga and the Instituto de Investigación Biomédica de Málaga y Plataforma en Nanomedicina-IBIMA Plataforma BIONAND.

Conflicts of Interest: The authors declare no conflicts of interest.

References

1. Nuclear Energy Agency (NEA). Chernobyl-Assessment of Radiological and Health Impacts, 2002. In *Update of Chernobyl: Ten Years On*; Organization for Economic Co-Operation and Development: Paris, France, 2002.
2. Nuclear Emergency Response Headquarters. Report of Japanese Government to the IAEA Ministerial. In Proceedings of the Conference on Nuclear Safety-The Accident at TEPCO's Fukushima Nuclear Power Stations, Tokyo, Japan, 15 September 2011; Technical Report; International Atomic Energy Agency: Tokyo, Japan, 2011.
3. Coeytaux, K.; Bey, E.; Christensen, D.; Glassman, E.S.; Murdock, B.; Doucet, C. Reported radiation overexposure accidents worldwide, 1980–2013: A systematic review. *PLoS ONE* **2015**, *10*, e0118709. [CrossRef] [PubMed]
4. Puerta-Ortiz, A.; Morales-Aramburo, J. Efectos biológicos de las radiaciones ionizantes. *Rev. Colomb. De Cardiol.* **2020**, *27*, 61–71. [CrossRef]
5. Dianov, G.; Lindahl, T. Reconstitution of the DNA base excision-repair pathway. *Curr. Biol.* **1994**, *4*, 1069–1076. [CrossRef] [PubMed]
6. Weinberg, R. Oncogenes and tumor suppressor genes. *CA Cancer J. Clin.* **1994**, *44*, 160–170. [CrossRef]
7. Weinberg, R. Finding the Anti-Oncogene. *Sci. Am.* **1988**, *259*, 44–53. [CrossRef]
8. Bender, M.; Gooch, P. Persistent chromosome aberrations in irradiated human subjects. *Radiat. Res.* **1962**, *16*, 44–53. [CrossRef]
9. Bender, M.; Gooch, P. Types and rates of X-ray-induced chromosome aberrations in human blood irradiated in vitro. *Proc. Natl. Acad. Sci. USA* **1962**, *48*, 522–532. [CrossRef]
10. Herate, C.; Sabatier, L. Retrospective biodosimetry techniques: Focus on cytogenetics assays for individuals exposed to ionizing radiation. *Mutat. Res. Mutat. Res.* **2020**, *783*, 108287. [CrossRef]
11. Sevan'kaev, A.; Khvostunov, I.; Mikhailova, G.; Golub, E.; Potetnya, O.; Shepel, N.; Nugis, V.Y.; Nadejina, N. Novel data set for retrospective biodosimetry using both conventional and FISH chromosome analysis after high accidental overexposure. *Appl. Radiat. Isot.* **2000**, *52*, 1149–1152. [CrossRef]
12. Ramalho, A.T.; Curado, M.; Natarajan, A. Lifespan of human lymphocytes estimated during a six year cytogenetic follow-up of individuals accidentally exposed in the 1987 radiological accident in Brazil. *Mutat. Res. Mol. Mech. Mutagen.* **1995**, *331*, 47–54. [CrossRef]
13. Ramalho, A.T.; Costa, M.L.P.; Oliveira, M.S. Conventional radiation-biological dosimetry using frequencies of unstable chromosome aberrations. *Mutat. Res. Mol. Mech. Mutagen.* **1998**, *404*, 97–100. [CrossRef] [PubMed]
14. Shen, X.; Ma, T.; Li, C.; Wen, Z.; Zheng, J.; Zhou, Z. High-precision automatic identification method for dicentric chromosome images using two-stage convolutional neural network. *Nat. Sci. Rep.* **2023**, *13*, 2124. [CrossRef] [PubMed]
15. Castro-Volio, I. Indicadores citogenéticos para la identificación de exposición a radiación ionizante en humanos. *Acta Médica Costarric.* **2013**, *55*, 110–117. [CrossRef]
16. Romm, H.; Oestreicher, U.; Kulka, U. Cytogenetic damage analysed by the dicentric assay. *Ann. Ist. Super Sanita.* **2009**, *45*, 251–259.
17. Hoffmann, W.; Schmitz-Feuerhake, I. How radiation-specific is the dicentric assay? *J. Expo. Sci. Environ. Epidemiol.* **1999**, *2*, 113–133. [CrossRef]
18. World Health Organization. *Cytogenetic Dosimetry: Applications in Preparedness for and Response to Radiation Emergencies*; Technical Report; International Atomic Energy Agency: Vienna, Austria, 2011.
19. Shen, X.; Qi, Y.; Ma, T.; Zhou, Z. A dicentric chromosome identification method based on clustering and watershed algorithm. *Sci. Rep.* **2019**, *9*, 2285. [CrossRef]
20. Rogan, P.K.; Li, Y.; Wickramasinghe, A.; Subasinghe, A.; Caminsky, N.; Khan, W.; Samarabandu, J.; Wilkins, R.; Flegal, F.; Knoll, J.H. Automating dicentric chromosome detection from cytogenetic biodosimetry data. *Radiat. Prot. Dosim.* **2014**, *159*, 95–104. [CrossRef]
21. Jeong, S.K.; Oh, S.J.; Kim, S.H.; Jang, S.; Kang, Y.R.; Kim, H.; Kye, Y.U.; Lee, S.H.; Lee, C.G.; Park, M.T.; et al. Dicentric chromosome assay using a deep learning-based automated system. *Sci. Rep.* **2022**, *12*, 22097. [CrossRef]
22. Kim, K.; Kim, K.S.; Jang, W.I.; Jang, S.; Hwang, G.T.; Woo, S.K. Deep Neural Network-Based Automatic Dicentric Chromosome Detection Using a Model Pretrained on Common Objects. *Diagnostics* **2023**, *13*, 3191. [CrossRef]
23. Wadhwa, A.S.; Tyagi, N.; Roy Chowdhury, P. Deep Learning based Automatic Detection of Dicentric Chromosome. *arXiv* **2022**, arXiv:2204.08029.

24. Molina-Cabello, M.A.; Accino, C.; López-Rubio, E.; Thurnhofer-Hemsi, K. Optimization of convolutional neural network ensemble classifiers by genetic algorithms. In Proceedings of the Advances in Computational Intelligence: 15th International Work-Conference on Artificial Neural Networks, IWANN 2019, Gran Canaria, Spain, 12–14 June 2019; Springer: Berlin/Heidelberg, Germany, 2019; pp. 163–173.
25. Molina-Cabello, M.A.; Elizondo, D.A.; Luque-Baena, R.M.; Lopez-Rubio, E. Foreground detection by ensembles of random polygonal tilings. *Expert Syst. Appl.* **2020**, *161*, 113518. [CrossRef]
26. Molina-Cabello, M.A.; Rodríguez-Rodríguez, J.A.; Thurnhofer-Hemsi, K.; López-Rubio, E. Histopathological image analysis for breast cancer diagnosis by ensembles of convolutional neural networks and genetic algorithms. In Proceedings of the 2021 International Joint Conference on Neural Networks (IJCNN), Virtual, 18–22 July 2021; pp. 1–8.
27. Léger, J.; Leyssens, L.; Kerckhofs, G.; De Vleeschouwer, C. Ensemble learning and test-time augmentation for the segmentation of mineralized cartilage versus bone in high-resolution microCT images. *Comput. Biol. Med.* **2022**, *148*, 105932. [CrossRef] [PubMed]
28. Jocher, G.; Chaurasia, A.; Qiu, J. Ultralytics YOLOv8. 2023. Available online: https://github.com/ultralytics/ultralytics (accessed on 10 November 2024).
29. Otsu, N. A Threshold Selection Method from Gray-Level Histograms. *IEEE Trans. Syst. Man Cybern.* **1979**, *9*, 62–66. [CrossRef]
30. RangeKing. *Brief Summary of YOLOv8 Model Structure*; GitHub: San Francisco, CA, USA, 2023.
31. Terven, J.; Córdova-Esparza, D.M.; Romero-González, J.A. A comprehensive review of yolo architectures in computer vision: From yolov1 to yolov8 and yolo-nas. *Mach. Learn. Knowl. Extr.* **2023**, *5*, 1680–1716. [CrossRef]
32. Rodríguez-Rodríguez, J.A.; López-Rubio, E.; Ángel-Ruiz, J.A.; Molina-Cabello, M.A. The Impact of Noise and Brightness on Object Detection Methods. *Sensors* **2024**, *24*, 821. [CrossRef]